Research Article

Ebrahem A. Algehyne, Showkat Ahmad Lone, Anwar Saeed, and Gabriella Bognár*

Analysis of the heat transfer enhancement in water-based micropolar hybrid nanofluid flow over a vertical flat surface

https://doi.org/10.1515/phys-2023-0201
received November 08, 2023; accepted January 29, 2024

Abstract: This article presented micropolar hybrid nanofluid flow comprising copper and alumina nanoparticles over a flat sheet. The mixed convection phenomenon is studied under the effect of gravity. Some additional forces such as magnetic field, thermal radiation, Eckert number, heat source, and thermal slip condition are adopted in this analysis. The leading equations are transformed into dimensionless format by employing appropriate variables and then evaluated by homotopy analysis method (HAM). The obtained results are compared with published results and found a good agreement with those published results. Also, the results of HAM are compared with those of numerical method and found a good agreement as well. The fluctuations within the flow profiles are showcased utilizing figures and tables, followed by an in-depth discussion and analysis. The outcomes of this work show that the higher volume fractions of copper and alumina nanoparticles improved the hybrid nanofluid viscosity, which results in the augmenting variation in the velocity profiles. The higher volume fractions of copper and alumina nanoparticles improved the hybrid nanofluid thermal conductivity, which results in the augmenting variation in thermal distribution. The growing mixed convection factor amplifies the buoyancy force toward the stagnation point flow, which enlarges the velocity panel. The effects of hybrid nanoparticles (Cu-Al_2O_3/water) at the surface are smaller on friction force and larger in case of thermal flow rate when compared to the nanofluids (Cu/water and Al_2O_3/water).

Keywords: micropolar fluid, hybrid nanofluid, mixed convection, thermal slip condition, stretching surface, HAM solution

*** Corresponding author: Gabriella Bognár**, Institute of Machine and Product Design, University of Miskolc, Miskolc-Egyetemvaros 3515, Miskolc, Hungary, e-mail: gabriella.v.bognar@uni-miskolc.hu
Ebrahem A. Algehyne: Department of Mathematics, Faculty of Science, University of Tabuk, P.O. Box 741, Tabuk 71491, Saudi Arabia; Nanotechnology Research Unit (NRU), University of Tabuk, Tabuk 71491, Saudi Arabia
Showkat Ahmad Lone: Department of Basic Sciences, College of Science and Theoretical Studies, Saudi Electronic University, Jeddah-M, Riyadh 11673, Saudi Arabia
Anwar Saeed: Department of Mathematics, Abdul Wali Khan University, Mardan, 23200, Khyber Pakhtunkhwa, Pakistan

1 Introduction

Micropolar fluid flow is a specialized study within fluid dynamics that considers fluids with both translational and microrotational motions at a microscopic level. The idea of this fluid was introduced by Eringin [1]. Unlike conventional fluids, which only account for translational momentum, micropolar fluids exhibit a unique behavior, where each fluid particle possesses an intrinsic angular momentum or microrotation [2]. This introduces an extra degree of freedom that significantly influences the overall flow characteristics. The governing equations of micropolar fluid dynamics extend the Navier–Stokes equations to incorporate microrotation effects, resulting in a more comprehensive representation of fluid behavior [3]. This augmentation leads to intricate flow patterns and enhanced vorticity due to the interaction between translational movement and microrotational tendencies. Applications of micropolar fluid flow encompass various fields, including biomechanics, microfluidics, and material processing, where the inclusion of microrotation provides a more accurate understanding of fluid–particle interactions [4,5]. Kocić *et al.* [6] inspected the thermal transportation of micropolar flow of fluid through a horizontal conduit and have noted that expansion in magnetic factor has retarded the velocity transportation and has supported the temperature distribution of fluid. Abbas *et al.* [7] inspected the effects of thermal and slip flow for micropolar fluid flow on a nonlinear Riga sheet. Ahmad *et al.* [8] inspected the thermal transmission for bio-convective micropolar fluid flow with viscous dissipative and microrotational characteristics and noted that concentration has augmented for progression in permeability factor, while upsurge in microrotational factor has caused augmentation in Nusselt number. Khan *et al.* [9] inspected the micropolar bio-convective fluid flow on a thin needle with dissipative and chemical reactivity effects and have noted that fluid concentration has retarded with the progression in chemical reactivity factor.

Heat transfer in nanofluid flow involves the exchange of thermal energy between a base fluid and nanoparticles suspended within it, driven by temperature differences. The indication of nanoparticle suspension in pure fluid was discussed first by Choi [10]. The enriched thermal conductivity of nanoparticles leads to better heat dissipation and transmission rates, making nanofluids promising for applications such as thermal exchangers, efficient cooling, and thermal management in electronics [11]. The altered flow behavior and improved conduction pathways offered by nanofluids contribute to their potential to enhance overall heat transfer performance, addressing challenges in diverse fields requiring efficient heat dissipation and regulation [12]. Shahid *et al.* [13] examined the activated energy for bio-convective nanoparticle flow on a penetrable sheet and noted that flow panel has weakened and thermal transportation has expanded with progression in nanoparticle concentration. Khan *et al.* [14] debated on thermal fluid flow for nanofluid through a conduit using impacts of microorganism. Bhatti *et al.* [15] examined microbes' impact on Williamson magnetohydrodynamics (MHD) nanofluid flow placed in a permeable medium. The enhanced thermal conductivity and altered flow behavior can lead to improved heat dissipation, making nanofluids attractive for applications such as electronics cooling, automotive radiators, and solar thermal systems [16]. One of the primary motivations for using nanofluids is the potential to significantly increase the thermal conductance of pure fluid. Anjum *et al.* [17] debated on MHD nanofluid flow on a plate with effect of microorganisms and examined that fluid thermal distribution has supported by nanoparticle concentration and magnetic effects. Upreti and Pandey [18] studied the tangent hyperbolic fluid flow past a stretching surface with Cattaneo–Christov heat flux model. Upreti *et al.* [19] examined the highly magnetized Casson nanofluid flow containing gold nanoparticle past a stretching surface. They examined different shapes of the gold nanoparticles and found that the cylindrical-shaped gold nanoparticle has greater influence on temperature profile compared to platelet and blade-shaped nanoparticles. Upreti *et al.* [20] investigated the stagnation point flow of Au-blood fluid past an extending sheet with suction/injection impacts. They examined different shapes of the Au nanoparticles and found that the blade-shaped Au nanoparticle has greater influence on temperature profile. Pandey and Upreti [21] investigated the two-dimensional nanofluid flow over a convectively heated stretching surface.

Hybrid nanofluid flow describes the behavior of a mixture that combines nanoscale particles and traditional fluids, creating a unique fluid medium with enhanced thermal properties. Nanofluids are engineered colloidal suspensions where nanoparticles are distributed in a pure fluid [22]. The introduction of nanoparticles can significantly modify the thermophysical and transportation characteristics of fluid. Sundar and Shaik [23] discussed the impacts of thermal transmission for diamond nanoparticle flow in a heat exchanger. Thermal flow in hybrid nanofluid flow is a complex phenomenon where the synergistic effects of combining several varieties of nanoparticles with a pure fluid lead to enhanced thermal conductivity and upgraded temperature transmission performance [24]. The incorporation of multiple nanoparticle types in the hybrid nanofluid further enhances this effect by utilizing their distinct thermal properties. This combination enables fine-tuning of the fluid's thermophysical characteristics to optimize heat transfer efficiency for specific applications, such as electronics cooling, automotive thermal management, and renewable energy systems [25]. Mahmood *et al.* [26] analyzed the hybrid nanofluid flow on a curved stretched sheet using magnetic effects and have noted that when suction factor varied from 2.0 to 2.5, the rate of heat flow has enlarged from 34 to 39%. Atashafrooz *et al.* [27] inspected the collective radiative–convective effects on thermal flow transportation for hybrid nanofluid flow on a surface. Raizah *et al.* [28] discussed the hybrid nanofluid flow in a conduit with impacts of activated energy, chemical reactivity, and Soret/Dufour effects. Latha *et al.* [29] addressed the stagnation point flow of a ternary hybrid nanofluid. They found that the skin friction and local Nusselt number are greatly influenced by the embedded factor as compared to hybrid and nanofluids. Prekash at al. [30] investigated the ternary hybrid nanofluid flow over a porous wedge under the influences of transverse magnetic and electric fields. They found that both the electric and magnetic fields' factors have declining impacts on the velocity profile of the ternary hybrid nanofluid flow. Further related studies can be seen in refs. [31–36].

The flow of fluid on stretching surface is a classical problem in fluid mechanics and has uses in various scientific areas. This problem involves the investigation of how a fluid flows on a sheet that is continuously stretching or contracting. Heat transference for flow of fluid on an extending surface involves the study of how heat is exchanged between a fluid and a surface that is continuously stretching or contracting [37]. The behavior of the thermal layer at boundary, influenced by stretching function of the surface, plays an essential role in thermal flow phenomenon [38]. The study of fluid flow on a stretching sheet is an active region of research, and researchers continue to explore different aspects of this problem, contributing to the area of dynamics of fluid and its applications. Bhatti *et al.* [39] computed the spectral relaxation for Maxwell fluid flow on a quadratic convection stretching surface and have observed that higher thermal relaxation factor and Prandtl number have retarded the thermal distribution. Alqatani *et al.* [40] inspected the mass and thermal transportation for MHD fluid flow on an extended sheet and found that the growth in suction parameter and the Darcy–Forchheimer effect significantly diminished the energy transfer rate of nanoliquids. Noor *et al.* [41] analyzed thermal flow for fluid flowing on a stretched sheet using the first- and second-order velocity slip constraints. Mahabaleshwar *et al.* [42] discussed the fluid axisymmetric flow on an elongated sheet and noted that skin friction has upsurge for a progression in magnetic factor. Sharma *et al.* [43] analyzed the fluid flow on an elongated sheet using chemical reactivity. Hussain and Sheremet [44] discussed the radiative and convective fluid flow on an extending surface using inclined magnetic effects.

In fluid dynamics, slip conditions for fluid flow on a surface play a significant role in thermal flow analysis. These conditions describe how the fluid molecules interact with the solid boundary and how their velocity is affected at the boundary. It is of worth mentioning that the choice of slip condition can have a substantial impression on the predicted performance of fluid flows, especially at micro- or nanoscales. In many practical applications, the no-slip condition is used because it simplifies the analysis and is appropriate for most macroscopic scenarios [45]. However, as the study of fluid dynamics at very small scales (nanofluidics) becomes more important, researchers are exploring the slip conditions to account for the unique behaviors that arise due to molecular interactions at the fluid–solid interface [46]. Patel *et al.* [47] tested the impacts of MHD on fluid flow on exponentially shrinking and enlarging sheet using slip condition and have noted that the skin friction coefficient has diminished across the contracting surface area, but conversely, the expanding surface has demonstrated an opposing impact as the velocity slip factor is augmented; meanwhile, the Nusselt number exhibited a contrary outcome. Zainodin *et al.* [48] discussed higher-order chemical reactivity slip constraint impacts on fluid flow on a Darcy medium and perceived that the existence of thermal and concentration slips caused a reduction in both mass and heat transmission rates, consequently resulting in a postponement of boundary-layer separation. Mahmood *et al.* [49] evaluated computationally the effects of MHD and slip constraints regarding nanofluid flow on shrinking and elongating sheet using heat sink/source. Yasin *et al.* [50] inspected experimentally the computational impacts of Hall current on fluid flow on a surface using slip constraints and Ohmic thermal effects. Ramzan *et al.* [51] compared a modeled based nanofluid flow with slip constraints and Darcy–Forchheimer effects and have revealed that the fluid temperature increased as the Eckert number and opposing buoyancy force increased, while it decreased with an elevation in the thermal jump parameter. Shahzadi *et al.* [52] discussed the impressions of slip conditions on ternary nanoparticles' blood flow in an artery for drug dispersal system.

Based on the upstairs observed literature, we are confident that there is very less work done on the stagnation point flow of hybrid nanofluid past a flat sheet. It is important to mention that in the present analysis, the surface has no stretching velocity at all; however, there is a free-stream velocity above the surface. Therefore, the authors examined the micropolar hybrid nanofluid flow on a flat surface. Water is taken as pure fluid, whereas copper and alumina nanoparticles are used to form the hybrid nanofluid. The analysis is considered under the impact of gravitational force, which we called the mixed convection phenomenon. Furthermore, the magnetic field, radiation, and heat source impacts are taken into consideration. The complete article is designed in section-wise, *i.e.*, problem is formulated in Section 2, with solution in Section 3 by homotopy analysis method (HAM). Section 4 shows the validation of the present results, Section 5 shows results/discussion, and Section 6 presents the conclusion.

2 Formulation of problem

Assume the 2D flow of a micropolar hybrid nanofluid comprising copper (Cu) and alumina (Al_2O_3) nanoparticles on a flat sheet. The flow is influenced by the magnetic field having strength B_0, which is applied normal to the flow direction. The fluid flow is considered in the x-direction, whereas the y-direction is taken perpendicularly. The flat surface has no stretching velocity at all, whereas the free stream velocity is $u_e = cx$ ($c > 0$ is constant). T, T_w, and T_∞ denote the fluid, surface, and free stream temperatures, respectively. Furthermore, the thermal slip condition is adopted to study the rate of heat transmission. The graphical view of fluid flow is depicted in Figure 1. Following are the flow assumptions:

- The stagnation point flow on a flat surface is adopted.
- The mixed convection phenomenon is adopted under the effect of gravity.
- Water is taken as pure fluid, whereas copper and alumina nanoparticles are used to form a hybrid nanofluid.
- Thermal radiation, heat source, and viscous dissipative effects are considered in the temperature equation.

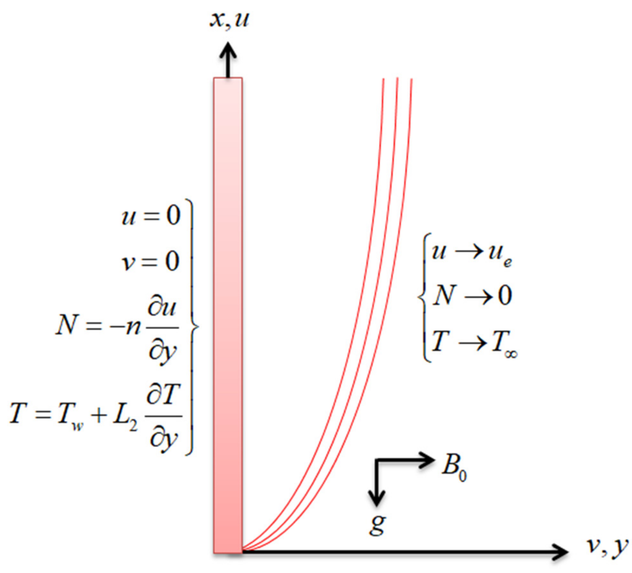

Figure 1: Flow configuration.

Keeping in mind the aforementioned assumptions, the leading equation are as follows [53,54]:

$$\frac{\partial u}{\partial x}+\frac{\partial v}{\partial y}=0, \tag{1}$$

$$\begin{aligned} u\frac{\partial u}{\partial x}+v\frac{\partial u}{\partial y}&=u_{\mathrm{e}}\frac{\mathrm{d}u_{\mathrm{e}}}{\mathrm{d}x}+\frac{\mu_{\mathrm{hnf}}}{\rho_{\mathrm{hnf}}}\left(1+\frac{K_1}{\mu_{\mathrm{hnf}}}\right)\frac{\partial^2 u}{\partial y^2}+\frac{K_1}{\rho_{\mathrm{hnf}}}\frac{\partial N}{\partial y}\\ &\quad-\frac{\sigma_{\mathrm{hnf}}}{\rho_{\mathrm{hnf}}}B_0^2(u-u_{\mathrm{e}})+g\frac{(\rho\beta_{\mathrm{T}})_{\mathrm{hnf}}}{\rho_{\mathrm{hnf}}}(T-T_\infty), \end{aligned} \tag{2}$$

$$u\frac{\partial N}{\partial x}+v\frac{\partial N}{\partial y}=\frac{\gamma_{\mathrm{hnf}}}{\rho_{\mathrm{hnf}}}\frac{\partial^2 N}{\partial y^2}-\frac{K_1}{\rho_{\mathrm{hnf}}\,j}\left(2N+\frac{\partial u}{\partial y}\right), \tag{3}$$

$$\begin{aligned} u\frac{\partial T}{\partial x}+v\frac{\partial T}{\partial y}&=\left(\frac{k_{\mathrm{hnf}}}{(\rho C_{\mathrm{p}})_{\mathrm{hnf}}}+\frac{1}{(\rho C_{\mathrm{p}})_{\mathrm{hnf}}}\frac{16\sigma^*T_\infty^3}{3k^*}\right)\frac{\partial^2 T}{\partial y^2}\\ &\quad+\frac{Q_0}{(\rho C_{\mathrm{p}})_{\mathrm{hnf}}}(T_{\mathrm{w}}-T_\infty)+\frac{\mu_{\mathrm{hnf}}}{(\rho C_{\mathrm{p}})_{\mathrm{hnf}}}\left(\frac{\partial u}{\partial y}\right)^2, \end{aligned} \tag{4}$$

with constraints at boundary:

$$\begin{aligned} &u=0, v=0, N=-n\frac{\partial u}{\partial y}, T=T_{\mathrm{w}}+L_2\frac{\partial T}{\partial y}, \quad \text{at} \quad y=0,\\ &\qquad u\to u_{\mathrm{e}}, N\to 0, T\to T_\infty, \quad \text{as} \quad y\to\infty. \end{aligned} \tag{5}$$

The flow components along the x and y-axes are u and v, N is the microrotation, T is the temperature, $\gamma_{\mathrm{hnf}}(=\mu_{\mathrm{hnf}}+K_1/2)j$ is the gyration gradient, K_1 is the material factor, j is the micro-inertia density, and n is the constant that lies between $[0,\ 1]$.

The thermophysical relations are given below with computation values in Table 1 [55–59]:

$$\left\{\begin{aligned} &\mu_{\mathrm{hnf}}=\frac{\mu_{\mathrm{f}}}{(1-\phi_1)^{2.5}(1-\phi_2)^{2.5}},\\ &\rho_{\mathrm{hnf}}=\rho_{s_2}\phi_2+\rho_{\mathrm{f}}(1-\phi_2)\left[(1-\phi_1)+\phi_1\frac{\rho_{\mathrm{s}_1}}{\rho_{\mathrm{f}}}\right],\\ &(\rho\beta_{\mathrm{T}})_{\mathrm{hnf}}=(\rho\beta_{\mathrm{T}})_{\mathrm{s}_2}\phi_2+(\rho\beta_{\mathrm{T}})_{\mathrm{f}}(1-\phi_2)\left[(1-\phi_1)\right.\\ &\qquad\left.+\phi_1\frac{(\rho\beta_{\mathrm{T}})_{\mathrm{s}_1}}{(\rho\beta_{\mathrm{T}})_{\mathrm{f}}}\right],\\ &(\rho C_{\mathrm{p}})_{\mathrm{hnf}}=(\rho C_{\mathrm{p}})_{\mathrm{s}_2}\phi_2+(\rho C_{\mathrm{p}})_{\mathrm{f}}(1-\phi_2)\left[(1-\phi_1)\right.\\ &\qquad\left.+\phi_1\frac{(\rho C_{\mathrm{p}})_{\mathrm{s}_1}}{(\rho C_{\mathrm{p}})_{\mathrm{f}}}\right],\\ &\frac{\sigma_{\mathrm{hnf}}}{\sigma_{\mathrm{nf}}}=\frac{\sigma_{\mathrm{s}_2}+2\sigma_{\mathrm{nf}}-2\phi_2(\sigma_{\mathrm{nf}}-\sigma_{\mathrm{s}_2})}{\sigma_{\mathrm{s}_2}+2\sigma_{\mathrm{nf}}+\phi_2(\sigma_{\mathrm{nf}}-\sigma_{\mathrm{s}_2})},\\ &\sigma_{\mathrm{nf}}=\sigma_{\mathrm{f}}\left\{\frac{\sigma_{\mathrm{s}_1}+2\sigma_{\mathrm{f}}-2\phi_1(\sigma_{\mathrm{f}}-\sigma_{\mathrm{s}_1})}{\sigma_{\mathrm{s}_1}+2\sigma_{\mathrm{f}}+\phi_1(\sigma_{\mathrm{f}}-\sigma_{\mathrm{s}_1})}\right\},\\ &\frac{k_{\mathrm{hnf}}}{k_{\mathrm{nf}}}=\frac{k_{\mathrm{s}_2}+2k_{\mathrm{nf}}-2\phi_2(k_{\mathrm{nf}}-k_{\mathrm{s}_2})}{k_{\mathrm{s}_2}+2k_{\mathrm{nf}}+\phi_2(k_{\mathrm{nf}}-k_{\mathrm{s}_2})},\\ &k_{\mathrm{nf}}=k_{\mathrm{f}}\left\{\frac{k_{\mathrm{s}_1}+2k_{\mathrm{f}}-2\phi_1(k_{\mathrm{f}}-k_{\mathrm{s}_1})}{k_{\mathrm{s}_1}+2k_{\mathrm{f}}+\phi_1(k_{\mathrm{f}}-k_{\mathrm{s}_1})}\right\}. \end{aligned}\right. \tag{6}$$

The following set of appropriate variables has used:

$$\begin{aligned} &u=cxf'(\xi),\quad v=-\sqrt{c\nu_{\mathrm{f}}}\,f(\xi),\quad \xi=\sqrt{\frac{c}{\nu_{\mathrm{f}}}}y,\\ &N=cx\sqrt{\frac{c}{\nu_{\mathrm{f}}}}g(\xi),\quad \theta(\eta)=\frac{T-T_{\mathrm{w}}}{T_{\mathrm{w}}-T_\infty}. \end{aligned} \tag{7}$$

Using Eq. (7), the transformed equations are as follows:

$$\begin{aligned} &\left(\frac{1+\eta_1K}{\eta_1}\right)f'''(\xi)+\eta_2(1+f'(\xi)f(\xi)-f'^2(\xi))+Kg'(\xi)\\ &\quad-M\eta_3(f'(\xi)-1)+\lambda\eta_4\theta(\xi)=0, \end{aligned} \tag{8}$$

$$\begin{aligned} &\left(\frac{2+\eta_1K}{2\eta_1}\right)g''(\xi)+\eta_2(f(\xi)g'(\xi)-g(\xi)f'(\xi))\\ &\quad-K(2g(\xi)+f''(\xi))=0, \end{aligned} \tag{9}$$

Table 1: Thermophysical features of nanoparticles and pure fluid [55–59]

Properties	H_2O	Cu	Al_2O_3
ρ	997.1	8,933	3,970
C_p	4,179	385	765
k	0.613	400	40
σ	0.05	5.96×10^{7}	1×10^{-10}
β_T	2.1×10^{-4}	7.65×10^{-5}	8.5×10^{-6}

$$\frac{1}{\eta_6}(\eta_5 + \mathrm{Rd})\theta''(\xi) + \frac{\eta_1}{\eta_6}\mathrm{EcPr}f''^2(\xi) + \frac{1}{\eta_6}\mathrm{Pr}Q\theta(\xi) = 0, \tag{10}$$

with boundary conditions:

$$\begin{aligned} &f'(\xi = 0) = 0, \quad f(\xi = 0) = 0,\\ &g(\xi = 0) = -nf''(\xi = 0), \quad \theta(\xi = 0) = 1 + \psi\theta'(\xi = 0),\\ &f'(\xi \to \infty) \to 1, \quad \theta(\xi \to \infty) \to 0, \quad H(\xi \to \infty) \to 0. \end{aligned} \tag{11}$$

In the aforementioned equations, K shows the micropolar factor, λ shows the mixed convection factor, Q represents the heat source factor, Pr signifies the Prandtl number, M shows the magnetic factor, Rd signifies the thermal radiation factor, and Ec is the Eckert number. These factors are defined as:

$$\begin{aligned} &\eta_1 = \frac{\mu_{\mathrm{f}}}{\mu_{\mathrm{hnf}}}, \quad \eta_2 = \frac{\rho_{\mathrm{hnf}}}{\rho_{\mathrm{f}}}, \quad \eta_3 = \frac{\sigma_{\mathrm{hnf}}}{\sigma_{\mathrm{f}}},\\ &\eta_4 = \frac{(\rho\beta_{\mathrm{T}})_{\mathrm{hnf}}}{(\rho\beta_{\mathrm{T}})_{\mathrm{f}}}, \quad \eta_5 = \frac{k_{\mathrm{hnf}}}{k_{\mathrm{f}}}, \quad \eta_6 = \frac{(\rho C_{\mathrm{p}})_{\mathrm{hnf}}}{(\rho C_{\mathrm{p}})_{\mathrm{f}}},\\ &K = \frac{K_1}{\mu_{\mathrm{f}}}, \quad \lambda = \frac{\mathrm{Gr_e}}{\mathrm{Re}_x^2}, \quad \mathrm{Gr_e} = \frac{g\beta_{\mathrm{T}}x^3(T_{\mathrm{w}} - T_\infty)}{v_{\mathrm{f}}^2},\\ &\mathrm{Re}_x = \frac{xu_{\mathrm{e}}}{v_{\mathrm{f}}}, \quad Q = \frac{Q_0}{a(\rho C_{\mathrm{p}})_{\mathrm{f}}},\\ &\mathrm{Pr} = \frac{v_{\mathrm{f}}(\rho C_{\mathrm{p}})_{\mathrm{f}}}{k_{\mathrm{f}}}, \quad M = \frac{\sigma_{\mathrm{f}}B_0^2}{a\rho_{\mathrm{f}}}, \quad \mathrm{Rd} = \frac{16\sigma^*T_\infty^3}{3k^*k_{\mathrm{f}}},\\ &\mathrm{Ec} = \frac{u_{\mathrm{e}}^2}{(C_{\mathrm{p}})_{\mathrm{f}}(T_{\mathrm{w}} - T_\infty)}, \end{aligned} \tag{12}$$

For engineering interest, the skin friction and Nusselt number are demarcated as:

$$\begin{aligned} C_{f_x} &= \frac{1}{\rho_{\mathrm{hnf}}u^2}\left((\mu_{\mathrm{hnf}} + K)\frac{\partial u}{\partial y} + KN\right)_{y=0},\\ \mathrm{Nu}_x &= -\left[\frac{x}{k_{\mathrm{f}}(T_{\mathrm{w}} - T_\infty)}\left(k_{\mathrm{hnf}}\frac{\partial T}{\partial y} + \frac{4\sigma^*}{3k^*}\frac{\partial T^4}{\partial y}\right)\right]_{y=0}. \end{aligned} \tag{13}$$

Using Eq. (7), we have

$$\begin{aligned} C_f &= C_{f_x}R_{\mathrm{e}}^{0.5} = \frac{1}{\eta_2}\left(\frac{1 + \eta_1(1 - n)K}{\eta_1}\right)f''(0),\\ \mathrm{Nu} &= \mathrm{Nu}_xR_{\mathrm{e}}^{-0.5} = -((\eta_5 + \mathrm{Rd}))\theta'(0). \end{aligned} \tag{14}$$

3 HAM solution

To solve the aforementioned nonlinear Eqs. (8)–(10) with boundary conditions (11), a semi-analytic approach HAM is utilized. For the proposed solution, we have used Mathematica 12.0 software. The initial guesses and linear operators are defined as:

$$f_0(\xi) = \xi - 1 + e^{-\xi}, \quad g_0(\xi) = 0 \quad \theta_0(\xi) = \left(\frac{1}{1 + \psi}\right)e^{-\xi}, \tag{15}$$

$$L_f(\xi) = f''' - f', \quad L_g(\xi) = g'' - g, \quad L_\theta(\xi) = \theta'' - \theta, \tag{16}$$

with properties:

$$\begin{aligned} &\{L_f(d_1 + d_2e^{-\xi} + d_3e^{\xi}) = 0, \quad L_g(d_4e^{-\xi} + d_5e^{\xi}) = 0,\\ &L_\theta(d_6e^{-\xi} + d_7e^{\xi}) = 0\}, \end{aligned} \tag{17}$$

where d_1–d_7 are the constants in general solution.

For the present model, the zeroth-order deformation is as follows:

$$\begin{aligned} &(1 - R)L_f[f(\xi;R) - f_0(\xi)](1 - R)\\ &\quad = R\chi_f\hbar_f[f(\xi;R), g(\xi, R), \theta(\xi, R)], \end{aligned} \tag{18}$$

$$\begin{aligned} &(1 - R)L_g[g(\xi;R) - g_0(\xi)](1 - R)\\ &\quad = R\chi_g\hbar_g[g(\xi;R), f(\xi;R)], \end{aligned} \tag{19}$$

$$\begin{aligned} &(1 - R)L_\theta[\theta(\xi;R) - \theta_0(\xi)](1 - R)\\ &\quad = R\chi_\theta\hbar_\theta[\theta(\xi;R), f(\xi;R)], \end{aligned} \tag{20}$$

along with boundary conditions:

$$\left\{\begin{array}{c} f(\xi;R) = 0, h(\xi;R) = -\eta f''(0),\\ f'(\xi;R) = 0, \theta(\xi;R) = 1 + \psi[(\xi;R)\theta']\}_{\xi=0},\\ f'(\xi;R) = 0, h(\xi;R) = 0, \theta(\xi;R) = 0\}_{\xi=\infty}. \end{array}\right\} \tag{21}$$

Here, $R = 0 \le R \le 1$ is the embedding parameter. Besides nonlinear operators χ_f, χ_H, and χ_θ are defined as:

$$\begin{aligned} &\chi_f(f(\xi;R), h(\xi;R), \theta(\xi;R))\\ &= \left(\frac{1 + \eta_1K}{\eta_1}\right)\frac{\partial^3 f(\xi;R)}{\partial\xi^3} + \eta_2\left(1 + f(\xi;R)\frac{\partial f(\xi;R)}{\partial\xi}\right.\\ &\left. - \left(\frac{\partial f(\xi;R)}{\partial\xi}\right)^2\right) + K\frac{\partial h(\xi;R)}{\partial\xi} - M\eta_3\left(\frac{\partial f(\xi;R)}{\partial\xi} - 1\right)\\ &+ \lambda\eta_4\frac{\partial\theta(\xi;R)}{\partial\xi}, \end{aligned} \tag{22}$$

$$\begin{aligned} &\chi_H(h(\xi;R), f(\xi;R))\\ &= \left(\frac{2 + \eta_1K}{2\eta_1}\right)\frac{\partial^2 h(\xi;R)}{\partial\xi^2} + \eta_2\left(f(\xi)\frac{\partial h(\xi;R)}{\partial\xi}\right.\\ &\left. - H(\xi)\frac{\partial f(\xi;R)}{\partial\xi}\right) - K\left(\frac{\partial^2 f(\xi;R)}{\partial\xi^2} - 2h(\xi;R)\right), \end{aligned} \tag{23}$$

$$\chi_\theta(\theta(\xi;R), f(\xi;R)) = \frac{1}{\eta_6}(\eta_6+\mathrm{Rd})\frac{\partial^2\theta(\xi;R)}{\partial\xi^2} + \frac{\eta_1}{\eta_6}\mathrm{EcPr}\left(\frac{\partial^2 f(\xi;R)}{\partial\xi^2}\right)^2 + \frac{1}{\eta_6}\mathrm{Pr}Q\theta(\xi;R). \tag{24}$$

By choosing $R = 1$ and $R = 0$, we obtain

$$\left.\begin{aligned} f(\xi;1) = f(\xi), g(\xi;1) = g(\xi), \theta(\xi;1) = \theta(\xi),\\ f(\xi;0) = f_0(\xi), g(\xi;0) = g_0(\xi), \theta(\xi;0) = \theta_0(\xi).\end{aligned}\right\} \tag{25}$$

Expanding by Taylor series for w.r.t. R, we have

$$\begin{aligned} f(\xi;R) &= f_0(\xi) + \sum_{r=1}^{\infty} f_r(\xi)R^r,\\ h(\xi;R) &= h_0(\xi) + \sum_{r=1}^{\infty} h_r(\xi)R^r,\\ \theta(\xi;R) &= \theta_0(\xi) + \sum_{r=1}^{\infty} \theta_r(\xi)R^r,\end{aligned} \tag{26}$$

where

$$\begin{aligned} f_r(\xi) &= \frac{1}{r!}\frac{\partial^r f(\xi;R)}{\partial R^r}\bigg|_{R=0},\\ h_r(\xi) &= \frac{1}{r!}\frac{\partial^r h(\xi;R)}{\partial R^r}\bigg|_{R=0},\\ \theta_r(\xi) &= \frac{1}{r!}\frac{\partial^r \theta(\xi;R)}{\partial R^r}\bigg|_{R=0}.\end{aligned} \tag{27}$$

The Yth-order deformation is as follows:

$$L_f[f_Y(\xi) - q_Y f_{Y-1}(\xi)] = \hbar_f \mathfrak{R}^f_Y(\xi), \tag{28}$$

$$L_g[g_Y(\xi) - q_Y g_{Y-1}(\xi)] = \hbar_g \mathfrak{R}^g_Y(\xi), \tag{29}$$

$$L_\theta[\theta_Y(\xi) - q_Y \theta_{Y-1}(\xi)] = \hbar_\theta \mathfrak{R}^\theta_Y(\xi), \tag{30}$$

Table 2: Solution of $f(\xi)$ for varying ξ keeping other factors as zero

ξ	Ashraf and Ashraf [53]	Das [54]	Present results
0.0	0.0	0.0	0.0
0.6	0.159171	0.159854	0.159568
1.2	0.555414	0.555403	0.555554
1.8	1.069900	1.067750	1.068654
2.4	1.635279	1.624300	1.624446
3.0	2.221620	2.212280	2.211435
3.6	2.816397	2.808153	2.808096
4.2	3.414474	3.410679	3.411246
4.8	4.013803	4.006367	4.009859
5.4	4.613592	4.606245	4.609869
6.0	5.213549	5.216228	5.214543

where

$$\begin{aligned}\mathfrak{R}^f_Y(\xi) = {} & \left(\frac{1+\eta_1 K}{2\eta_1}\right) f'''_{Y-1} - \eta_3 M\left(\sum_{n=0}^{Y-1} f'_{Y-1} - 1\right)\\ & + \eta_2\left(\sum_{n=0}^{Y-1} f_{Y-1-n} f''_n - \sum_{n=0}^{Y-1} f'_{Y-1-n} f'_n + 1\right) + K\sum_{n=0}^{Y-1} g'_{Y-1}\\ & + \lambda\eta_4 \sum_{n=0}^{Y-1}\theta'_{Y-1},\end{aligned} \tag{31}$$

$$\begin{aligned}\mathfrak{R}^g_Y(\xi) = {} & \left(\frac{2+\eta_1 K}{2\eta_1}\right) g''_{Y-1} + \eta_2\left(\sum_{n=0}^{Y-1} f_{Y-1-n} g'_n - \sum_{n=0}^{Y-1} g_{Y-1-n} f'_n\right)\\ & - K\sum_{n=0}^{Y-1} f''_{Y-1} - 2\sum_{n=0}^{Y-1} g_{Y-1},\end{aligned} \tag{32}$$

$$\begin{aligned}\mathfrak{R}^\theta_Y(\xi) = {} & \frac{1}{\eta_6}(\eta_6 + \mathrm{Rd})\theta''_{Y-1} + \frac{\eta_1}{\eta_6}\mathrm{EcPr}\sum_{n=0}^{Y-1} f''_{Y-1-n} f''_n\\ & + \frac{1}{\eta_6}\mathrm{Pr}Q\sum_{n=0}^{Y-1}\theta_{Y-1}.\end{aligned} \tag{33}$$

The boundary conditions are as follows:

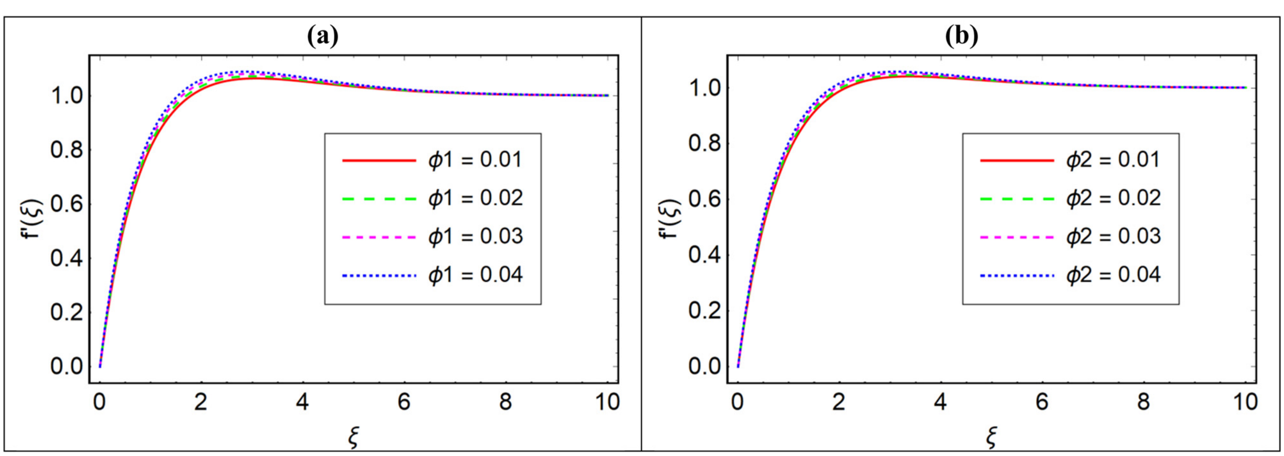

Figure 2: (a and b) Impacts of ϕ_1 and ϕ_2 on $f'(\xi)$.

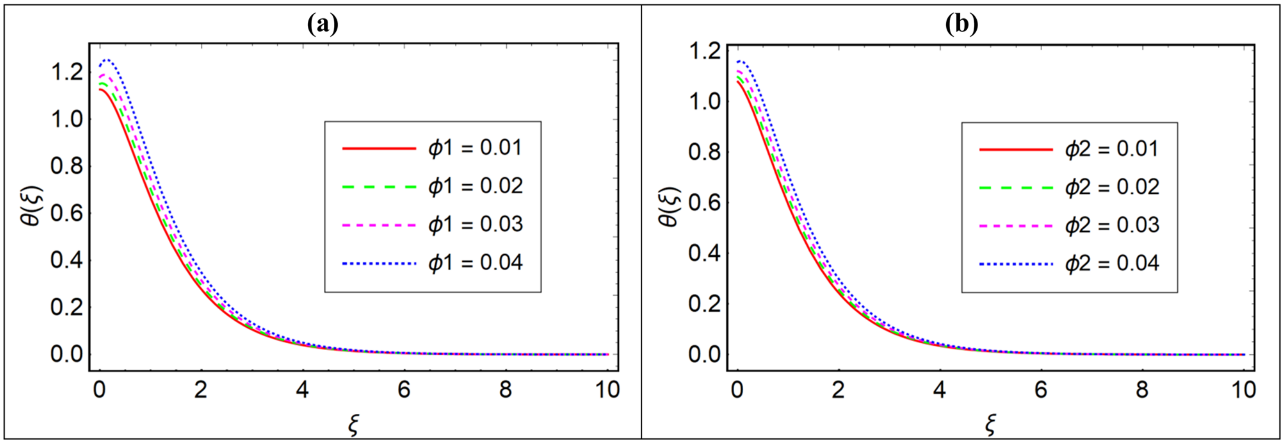

Figure 3: (a and b) Impacts of ϕ_1 and ϕ_2 on $\theta(\xi)$.

$$\left.\begin{cases} f_Y(0) = 0, \quad f_Y'(0) = 0, \quad g_Y(0) = -\eta f_Y''(0), \\ \theta_Y(0) = [\psi\theta_Y'(0) + 1], \\ f_Y'(\infty) = 1, \quad g_Y(\infty) = 0, \quad \theta_Y(\infty) = 0, \end{cases}\right\}, \tag{34}$$

where

$$q_Y = \begin{cases} 0, & \text{if} \quad R \le 1 \\ 1, & \text{if} \quad R > 1. \end{cases} \tag{35}$$

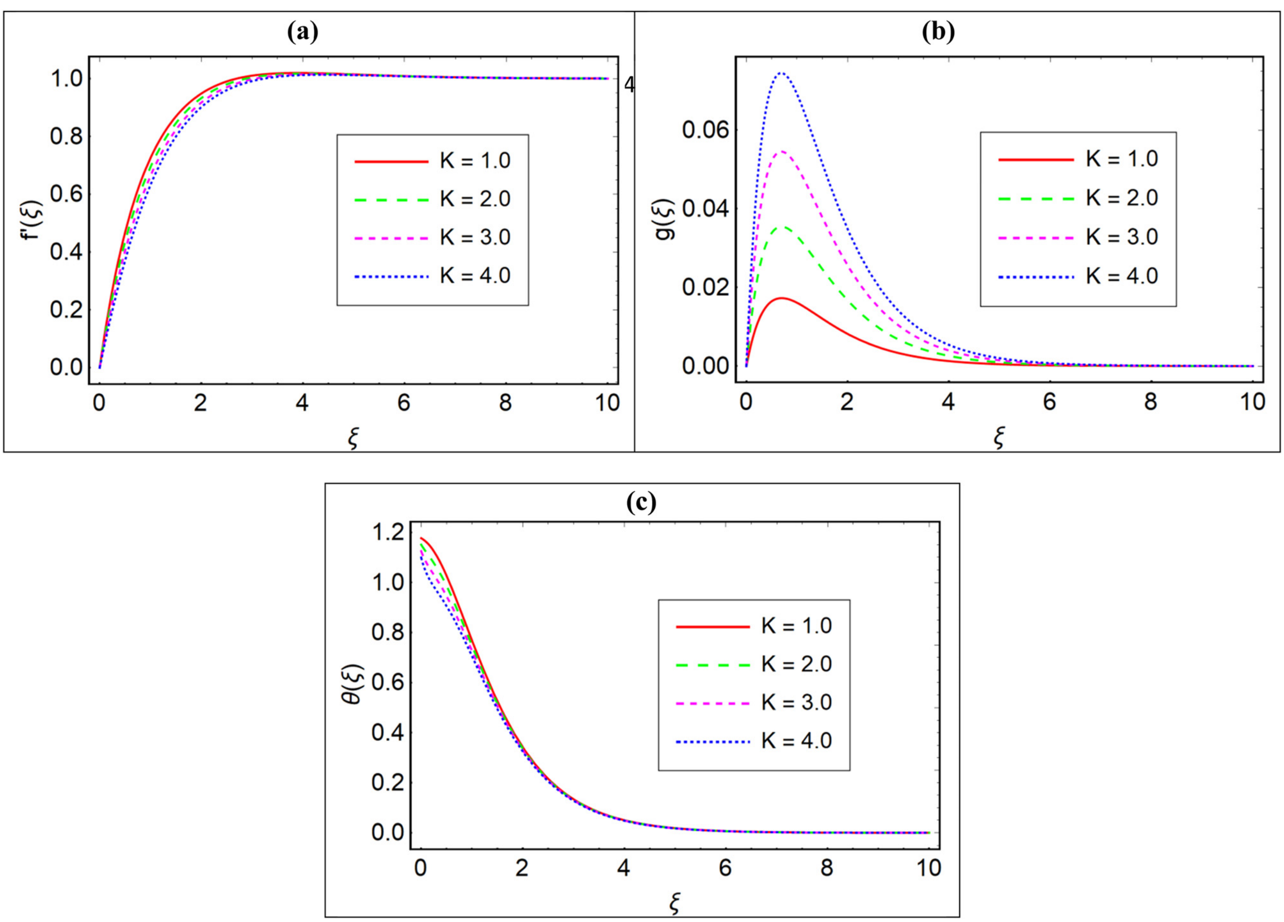

Figure 4: (a–c) Impact of K on $f'(\xi)$, $g(\xi)$, and $\theta(\xi)$.

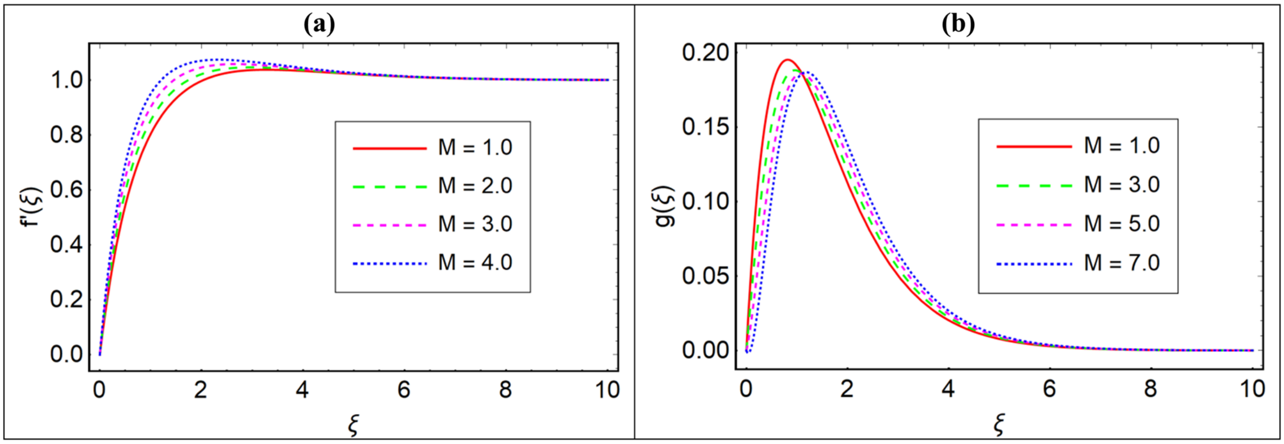

Figure 5: (a and b) Impact of M on $\theta(\xi)$ and $g(\xi)$.

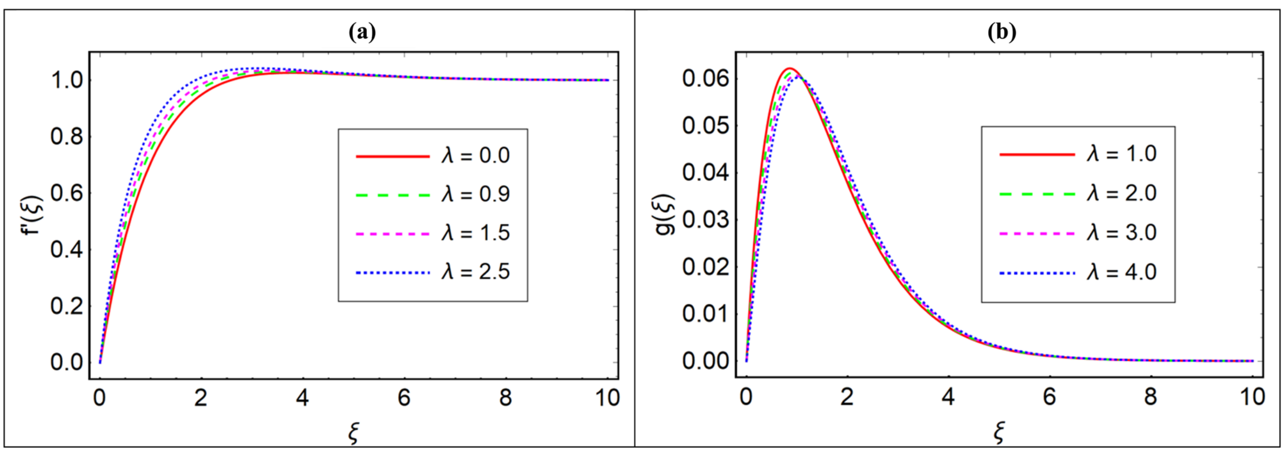

Figure 6: (a and b) Impact of λ on $f'(\xi)$ and $g(\xi)$.

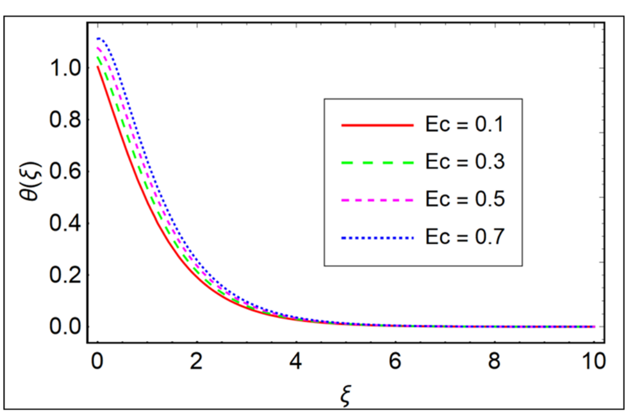

Figure 7: Impact of Ec on $\theta(\xi)$.

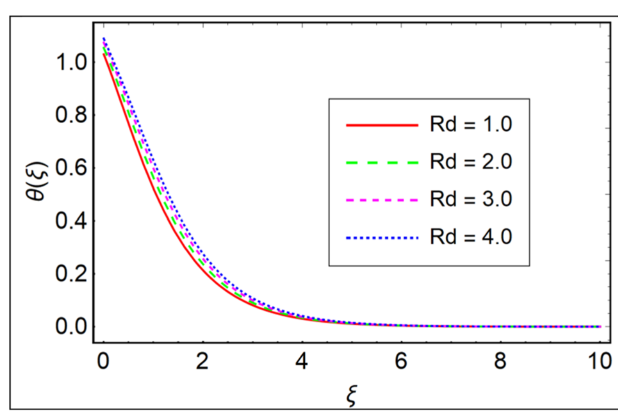

Figure 8: Impact of Rd on $\theta(\xi)$.

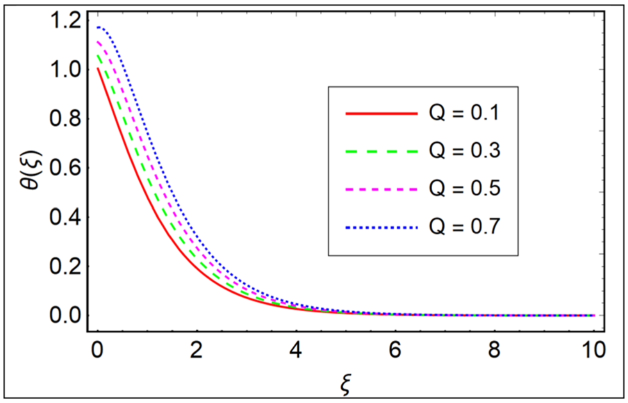

Figure 9: Impact of Q on $\theta(\xi)$.

4 Validation

To validate the present solution with those of the published results by Mahabaleshwar *et al.* [42], Table 2 is presented. This solution is compared with those established results and has found a very close solution in the present analysis. Thus, we confirm that the solution of the present model is valid.

5 Discussion of results

This section presents the physical discussion about the obtained results. The obtained results are displayed in

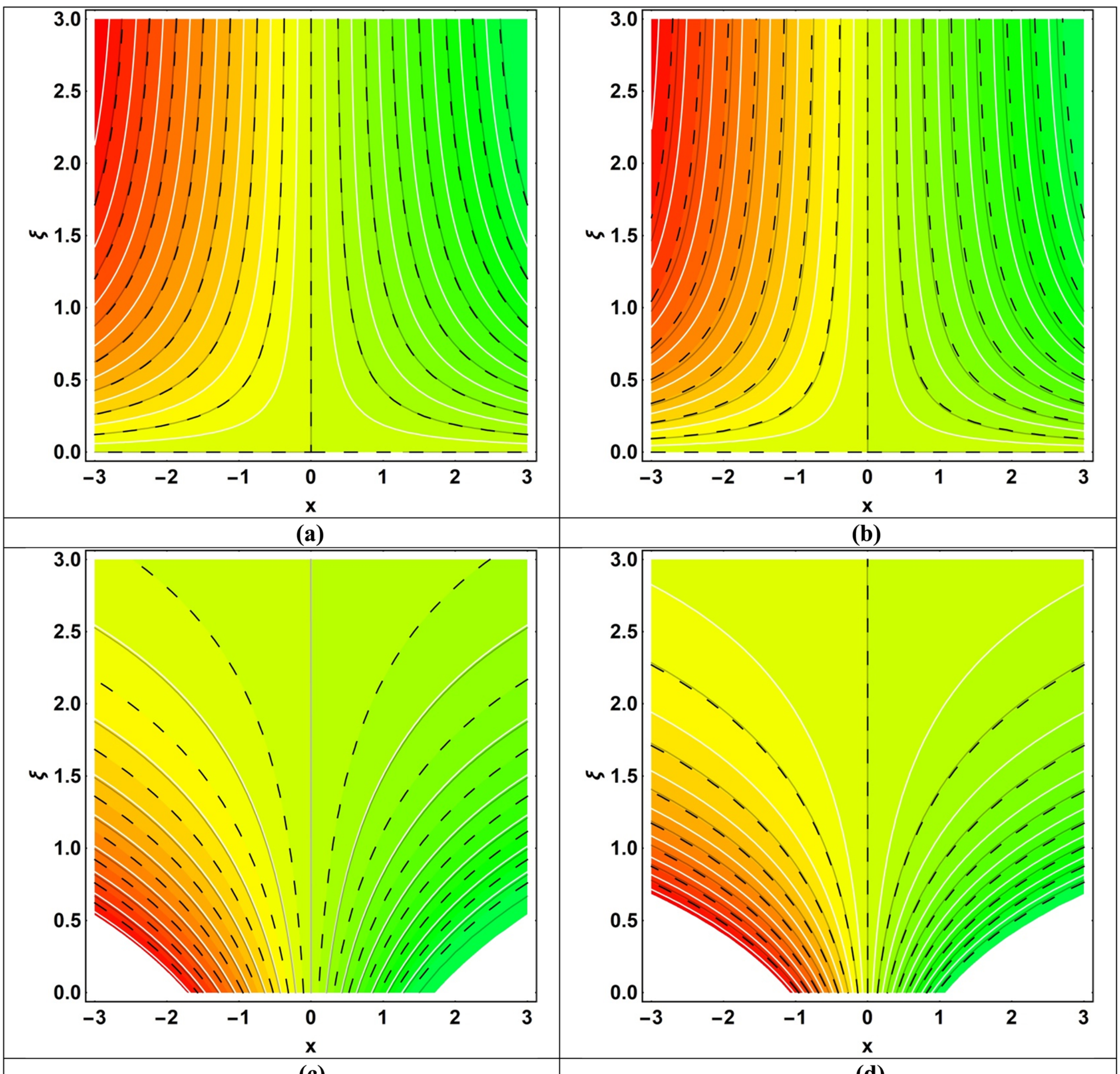

Figure 10: (a) Streamlines when $K = 0$, (b) streamlines when $K = 1$, (c) contour lines when $K = 0$, and (d) contour lines when $K = 1$.

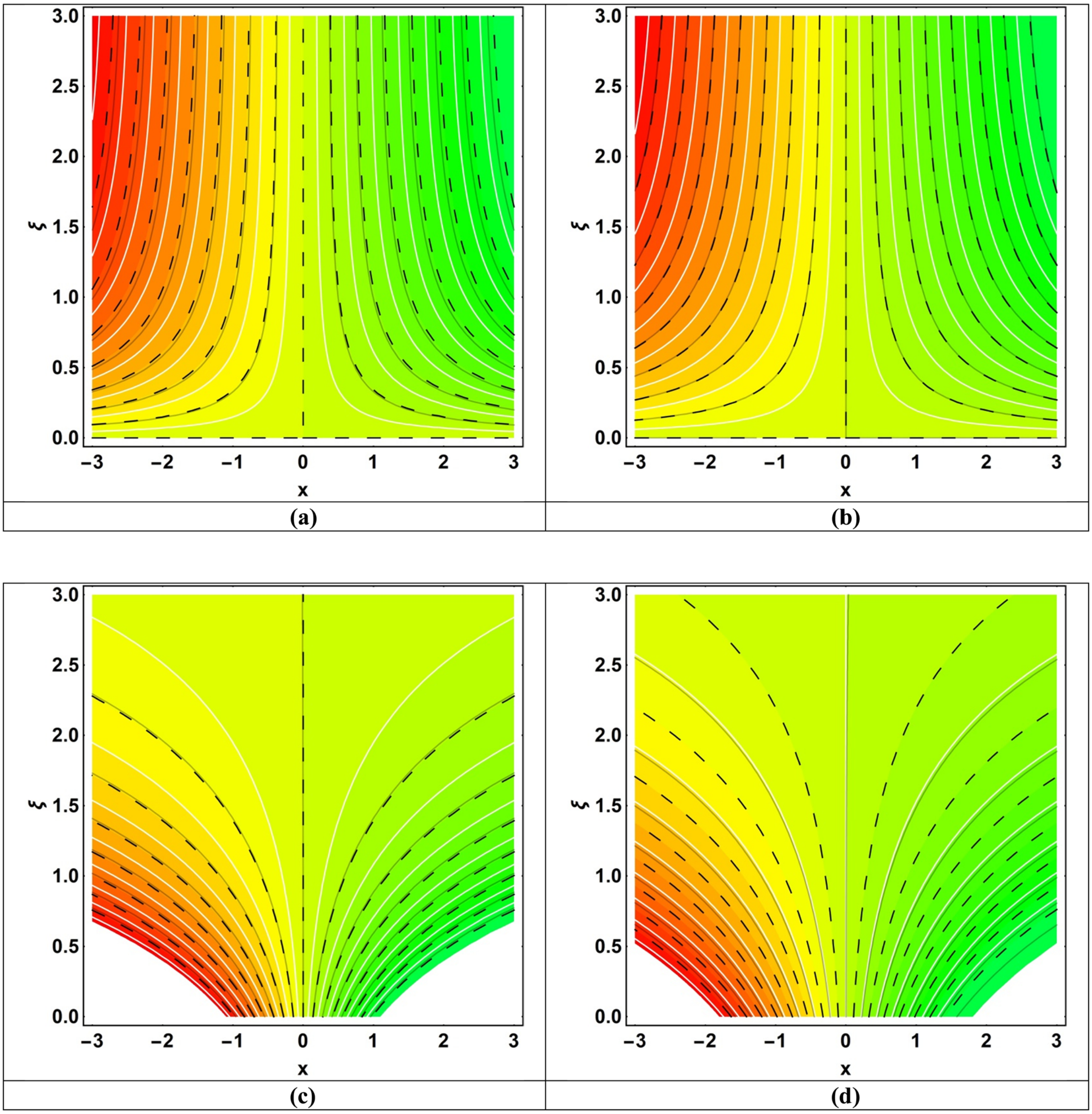

Figure 11: (a) Streamlines when M = 0, (b) streamlines when M = 10, (c) contour lines when M = 0, and (d) contour lines when M = 10.

Figures 2–12 and Tables 3–7. The default values of the embedded factor are chosen as $K = 0.5$, $\lambda = 0.5$, $Q = 0.2$, $\mathrm{Pr} = 6.2$, $M = 1.2$, $\mathrm{Rd} = 0.3$, $\mathrm{Ec} = 0.1$, $\phi_1 = 0.04$, and $\phi_2 = 0.04$. Figure 2(a) and (b) depicts the deviations in velocity profiles *via* nanoparticle volume fractions of the Cu (ϕ_1) and Al_2O_3 (ϕ_2) nanoparticles, respectively. From both the figures, we see that the velocity profiles increase against ϕ_1 and ϕ_2. The reason is that growth in volume fraction and the fluid viscosity improves. In this process, the density of fluid upsurge offers more resistivity to fluid flow. Thus, in the present case, both ϕ_1 and ϕ_2 enhance the water-based hybrid nanofluid flow viscosity, which, as a result, reduces the velocity panels. Figure 3(a) and (b) displays the variation in temperature profiles *via* nanoparticle volume fractions of the Cu (ϕ_1) and Al_2O_3 (ϕ_2) nanoparticles, respectively. From both figures, it has revealed that temperature profiles intensify against ϕ_1 and ϕ_2. This is because when more solid particles are suspended in

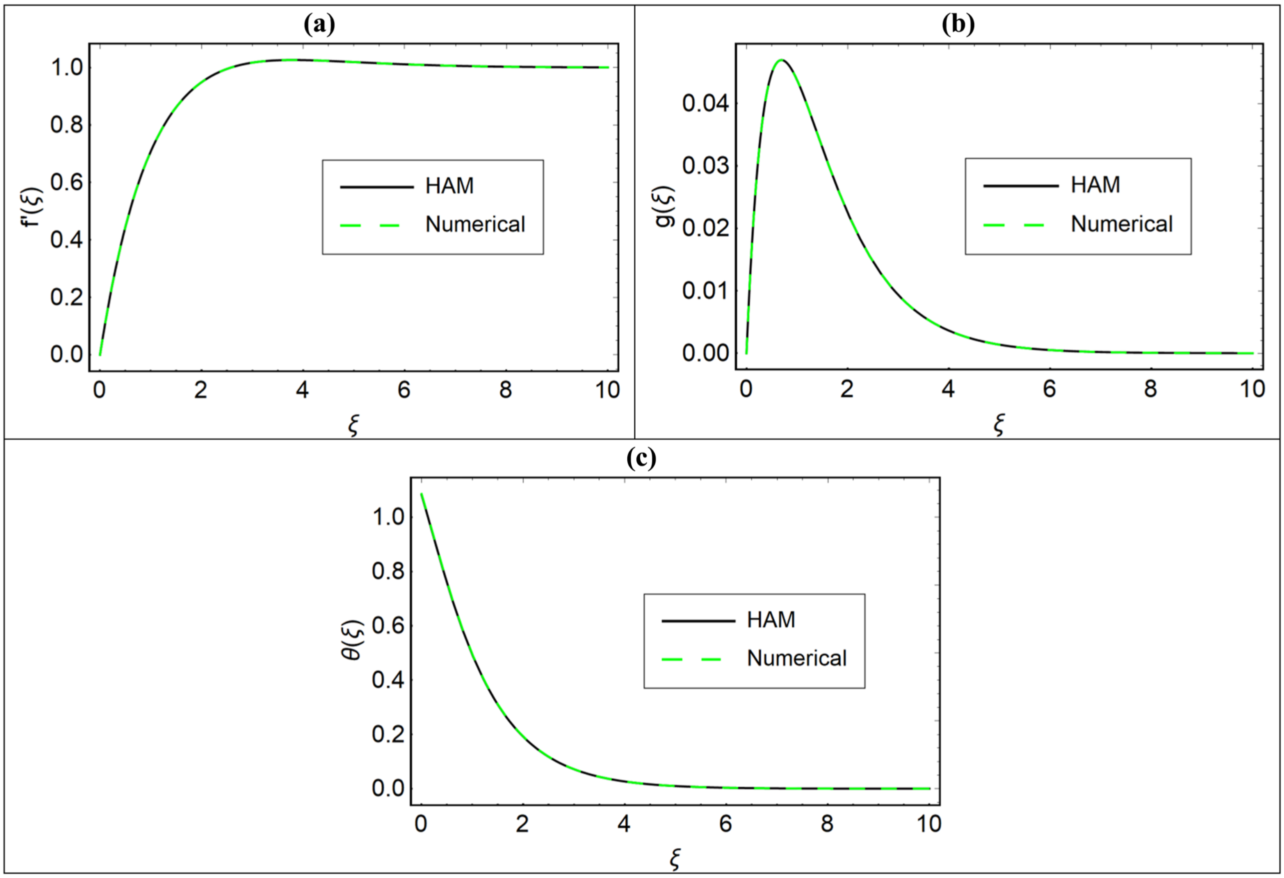

Figure 12: (a–c) Comparison of the HAM and numerical solutions for $f'(\xi)$, $g(\xi)$, and $\theta(\xi)$.

pure fluid, the thermal conductivity of the fluid improves, increasing the heat transmission. The stiffening of the thermal layer at boundary is caused by this rise in temperature profiles. Comparing both the figures, we see that the larger impact of volume fraction of the solid nanoparticle on thermal panels is revealed for Cu–water nanofluid as of Al_2O_3–water. Actually, copper nanoparticle has better thermal conductance than the alumina nanoparticle. Thus, the highest impact is found in Figure 3(a). Figure 4(a) and (c) demonstrates the impression of micropolar parameter (K) on $f'(\xi)$, $g(\xi)$, and $\theta(\xi)$, respectively. It can be noted that as the micropolar factor escalates, the velocity and temperature profiles experience a decrease. On the other hand, the microrotation velocity profile increases with the growth in micropolar factor. The reason is that the micropolar factor diminishes the dynamic viscosity of fluid, which consequently increases the microrotation velocity profile with the increasing micropolar factor. Figure 5(a) and (b) shows that higher magnetic factor escalates the flow panels. Conversely, the higher magnetic has dual nature for the microrotation profile. On the sheet's surface, an elevated magnetic factor amplifies the counteracting force, leading to a decrease in the microrotation profile, while above the surface, the opposing force diminishes and the microrotation profile gets increase. Generally, the magnetic factor produces the Lorentz force that plays against the flow of liquid. This is only applicable for stretching sheet. In the present case, there is no stretching velocity of the sheet at all. Of course, there is an ambient velocity due to the presence of stagnation point. Figure 6(a) and (b) displays the outcome of mixed convection factor on velocity and microrotation panels. Growth in velocity distribution is noted for upsurge in λ as portrayed in Figure 6(a). Actually, increasing mixed convection factor amplifies the buoyancy force toward the stagnation point flow, which enlarges the width of momentum layer at boundary. Therefore, the higher λ escalates $f'(\xi)$. On the other hand, a dual impact of λ on microrotation profile is depicted. Near the surface of flat sheet, the buoyancy force increases the microrotation profile, while at some distance from the sheet surface, this effect behaves oppositely. Figure 7 shows the Ec effects on $\theta(\xi)$ with a growing behavior of $\theta(\xi)$. It is shown that the width of thermal layer at boundary and temperature profiles improves as Ec increases. Physically, it is

Table 3: Comparison of the HAM and numerical methods for $f'(\xi)$

ξ	$f'(\xi)$	
	HAM	Numerical
0.0	2.78×10^{-17}	2.78×10^{-17}
0.5	0.450228	0.452234
1.0	0.713433	0.715388
1.5	0.865786	0.867243
2.0	0.951572	0.952556
2.5	0.996976	0.997609
3.0	1.018325	1.018723
3.5	1.025983	1.026229
4.0	1.026412	1.026563
4.5	1.02348	1.023572
5.0	1.019374	1.019430
5.5	1.015233	1.015268
6.0	1.011575	1.011596
6.5	1.008573	1.008586
7.0	1.006224	1.006231
7.5	1.004445	1.004450
8.0	1.003133	1.003136
8.5	1.002184	1.002185
9.0	1.001507	1.001509
9.5	1.001032	1.001033
10.0	1.000701	1.000702

Table 4: Comparison of the HAM and numerical methods for $g(\xi)$

ξ	$g(\xi)$	
	HAM	Numerical
0.0	2.78×10^{-17}	2.78×10^{-17}
0.5	0.044816	0.044782
1.0	0.043734	0.043730
1.5	0.032915	0.032925
2.0	0.022511	0.022523
2.5	0.014693	0.014703
3.0	0.009343	0.009350
3.5	0.005848	0.005853
4.0	0.003623	0.003626
4.5	0.002230	0.002232
5.0	0.001366	0.001367
5.5	0.000834	0.000835
6.0	0.000508	0.000509
6.5	0.000309	0.000310
7.0	0.000188	0.000188
7.5	0.000114	0.000114
8.0	6.94×10^{-5}	6.94×10^{-5}
8.5	4.21×10^{-5}	4.21×10^{-5}
9.0	2.55×10^{-5}	2.56×10^{-5}
9.5	1.55×10^{-5}	1.55×10^{-5}
10.0	9.4×10^{-10}	9.41×10^{-10}

Table 5: Comparison of the HAM and numerical methods for $\theta(\xi)$

ξ	$\theta(\xi)$	
	HAM	Numerical
0.0	1.082509	1.085835
0.5	0.758072	0.760936
1.0	0.492794	0.494739
1.5	0.310022	0.311254
2.0	0.191899	0.192660
2.5	0.117761	0.118225
3.0	0.071917	0.072200
3.5	0.043798	0.043970
4.0	0.026630	0.026734
4.5	0.016176	0.016239
5.0	0.009820	0.009858
5.5	0.005959	0.005983
6.0	0.003616	0.003630
6.5	0.002193	0.002202
7.0	0.001331	0.001336
7.5	0.000807	0.000810
8.0	0.000490	0.000491
8.5	0.000297	0.000298
9.0	0.000180	0.000181
9.5	2.09×10^{-5}	2.11×10^{-5}
10.0	6.63×10^{-10}	6.65×10^{-10}

discovered that Ohmic heating effect results in a rise in temperature of fluid and, as a result, a reduction in thermal flow. Furthermore, it is discovered that viscous heating has an impact on temperature, with the occurrence of a stronger impact magnetic field. Figure 8 shows the impression of Rd on $\theta(\xi)$. From this figure, it is perceived that the higher values of Rd increase $\theta(\xi)$. The thermal radiation factor

Table 6: Impacts of ϕ_1, ϕ_2, $\phi_1 = \phi_2$, M, and K on C_f

ϕ_1	ϕ_2	M	K	C_f
0.04	0.0	0.5	0.5	0.723974
0.05				0.647360
0.06				0.579946
0.0	0.04			0.927634
	0.05			0.877409
	0.06			0.830391
0.04	0.04			0.577452
0.05	0.05			0.489587
0.06	0.06			0.415749
0.04	0.04	0.2		0.635134
		0.3		0.615907
		0.4		0.596679
		0.5	0.2	0.410437
			0.3	0.463797
			0.4	0.519461

Table 7: Impacts of ϕ_1, ϕ_2, $\phi_1 = \phi_2$, Rd, Ec, Q, and ψ on Nu

ϕ_1	ϕ_2	Rd	Ec	Q	ψ	Nu
0.01	0.0	0.3	0.1	0.3	0.2	1.66916
0.02						1.73014
0.03						1.79444
0.0	0.01					1.66663
	0.02					1.72481
	0.03					1.78603
0.01	0.01					1.82924
0.02	0.02					1.91029
0.03	0.03					2.00660
0.04	0.04	0.3				2.17084
		0.4				2.35076
		0.5				2.53313
		0.3	0.2			2.29782
			0.3			2.42483
			0.4			2.55184
			0.1	0.1		1.97354
				0.2		2.07217
				0.3		2.17084
				0.3	0.3	1.81323
					0.4	1.50284
					0.5	1.23022

escalates the heat of the flow system that causes augmentation in thermal profiles. Therefore, higher Rd heightens the temperature profile. Similarly, the consequence of heat source factor Q on thermal profile is exposed in Figure 9. Also, an increasing impact is observed here. The reason is that the higher heat source increases the heat transfer rate, which consequently increases the thermal boundary-layer thickness and temperature profile as well. Thus, higher Q increases $\theta(\xi)$. Figure 10(a)–(d) shows the streamlines and contour lines of the hybrid nanofluid for $K = 0$ and $K = 1$, respectively. From Figure 11(a) and (b), we observed that the streamlines become closer to each other when $K = 1$ as compared to $K = 0$, since the higher K increases the dynamic viscosity, which results in higher friction force at the sheet surface, and as a result, the streamlines become closer to each other. Also, when the dynamic viscosity increases with higher K, the boundary-layer thickness reduces as well. This effect is observed in Figure 10(c) and (d). Figure 11(a)–(d) shows the streamlines and contour lines of the hybrid nanofluid for $M = 0$ and $M = 10$, respectively. From Figure 11(a) and (b), we observed that the streamlines become apart from each other when $M = 10$ as compared to $M = 0$ since the higher M increases the velocity profile due to reducing friction force at the sheet surface. Thus, streamlines become apart from each other. Also, when the skin friction reduces with higher M, the boundary-layer thickness increases as well. This effect is observed in Figure 11(c) and (d). Figure 12(a)–(c) and Tables 3–5 show the comparison of the HAM and numerical solutions for $f'(\xi)$, $g(\xi)$, and $\theta(\xi)$. Form these figures and tables, we see that both the semi-analytical and numerical methods have close relation. Table 6 shows the impacts of ϕ_1, ϕ_2, $\phi_1 = \phi_2$, M, and K on C_f. From this table, it is perceived that nanoparticle volume fraction diminishes C_f. The reason is explained in the above figures. Here, the important point is that the effect is smaller for the case of hybrid nanofluid flow (Cu-Al_2O_3/water) when compared to the nanofluids (Cu/water and Al_2O_3/water). Furthermore, upsurge in M diminishes the friction force at the surface, while the greater micropolar factor escalates it at the surface of the flat. Table 7 displays the effects of ϕ_1, ϕ_2, $\phi_1 = \phi_2$, Rd, Ec, Q, and ψ on Nu. This table demonstrates that growth in nanoparticle volume fractions and heat transfer rate. Actually, upsurge in ϕ_1 and ϕ_2 increases the thermal conductivities of the nanofluids. The important point is here to mention that the heat transfer rate of the hybrid nanofluid is more than that of nanofluids. Furthermore, the Eckert number, thermal radiation, and heat source factors escalate the thermal flow rate, while the thermal slip reduces the heat transfer rate.

6 Conclusion

In this article, we have studied the micropolar hybrid nanofluid containing copper (Cu) and alumina (Al_2O_3) nanoparticles past a flat surface. The mixed convection phenomenon is studied under the effect of gravity. Some additional forces such as magnetic field, thermal radiation, Eckert number, heat source, and thermal slip condition are adopted in the present analysis. The HAM is applied for the solution of the present analysis, which is validated with those of published results and a numerical method. On the completion of this analysis, the following concluding points are extracted:

- The higher volume fractions of copper and alumina nanoparticles improved the hybrid nanofluid viscosity, which results in the augmenting variation in the velocity profiles.
- The higher volume fractions of copper and alumina nanoparticles improved the hybrid nanofluid thermal conductivity, which results in the augmenting variation in the temperature profiles and heat transfer.
- The micropolar factor has increased the dynamic viscosity of the hybrid nanofluid flow, which, as a result, increases the microrotation velocity profile. On the other hand, the micropolar factor has declining impacts on the velocity and temperature profiles.
- The increasing mixed convection factor amplifies the buoyancy force toward the stagnation point flow, which enlarges the momentum boundary-layer thickness, and as a result, the velocity profile gets improved.

- The higher Eckert number, thermal radiation, and heat source factor have increased the temperature profiles of the hybrid nanofluid flow.
- The effects of the volume fractions of copper and alumina nanoparticles on friction force at the surface are smaller for the case of hybrid nanofluid flow (Cu-Al_2O_3/water) when compared to the nanofluids (Cu/water and Al_2O_3/water).
- The effects of the volume fractions of copper and alumina nanoparticles on heat transfer rates are higher for the case of hybrid nanofluid flow (Cu-Al_2O_3/water) when compared to the nanofluids (Cu/water and Al_2O_3/water).

7 Future recommendations

In the future, the present model can be extended for a three-dimensional stagnation point flow of a micropolar fluid containing different types of nanoparticles such as CuO, Fe_2O_3, Fe_3O_4, and TiO_2. Also, some different types of base fluids that exhibit Newtonian behavior can be considered in future work. The fluid flow can be examined by adopting the velocity slip, thermal convective, mass flux, and zero-mass flux conditions in the future.

Funding information: This study was supported by Project No. 129257 implemented with the support provided from the National Research, Development and Innovation Fund of Hungary, financed under the K 18 funding scheme.

Author contributions: All authors have accepted responsibility for the entire content of this manuscript and approved its submission.

Conflict of interest: The authors state no conflict of interest.

Data availability statement: The data that support the findings of this study are available from the corresponding author upon a reasonable request.

References

[1] Eringen AC. Theory of micropolar fluids. J Math Mech. 1966;16:1–18. http://www.jstor.org/stable/24901466.
[2] Alzahrani J, Vaidya H, Prasad KV, Rajashekhar C, Mahendra DL, Tlili I. Micro-polar fluid flow over a unique form of vertical stretching sheet: Special emphasis to temperature-dependent properties. Case Stud Therm Eng. 2022;34:102037.
[3] Raza A, Ul Haq R, Shah SS, Alansari M. Existence of dual solution for micro-polar fluid flow with convective boundary layer in the presence of thermal radiation and suction/injection effects. Int Commun Heat Mass Transf. 2022;131:105785.
[4] Lone SA, Alyami MA, Saeed A, Dawar A, Kumam P, Kumam W. MHD micropolar hybrid nanofluid flow over a flat surface subject to mixed convection and thermal radiation. Sci Rep. 2022;12:1–14.
[5] Swalmeh MZ, Shatat F, Alwawi FA, Ibrahim MAH, Sulaiman IM, Yaseen N, et al. Effectiveness of radiation on magneto-combined convective boundary layer flow in polar nanofluid around a spherical shape. Fractal Fract. 2022;6:383.
[6] Kocić M, Stamenković Ž, Petrović J, Bogdanović-Jovanović J. Control of MHD Flow and Heat Transfer of a Micropolar Fluid through Porous Media in a Horizontal Channel. Fluids. 2023;8:93.
[7] Abbas N, Shatanawi W, Rehman KU, Shatnawi TA. Velocity and thermal slips impact on boundary layer flow of micropolar nanofluid over a vertical nonlinear stretched Riga sheet. Proc Inst Mech Eng Part N J Nanomater Nanoeng Nanosyst. 2023;23977914231156684.
[8] Ahmad B, Bibi S, Khan SU, Abbas T, Raza A. Bioconvective thermal transport of micropolar nanofluid with applications of viscous dissipation and micro-rotational features. Waves Random Complex Media. 2023;1–19.
[9] Khan A, Saeed A, Tassaddiq A, Gul T, Mukhtar S, Kumam P, et al. Bio-convective micropolar nanofluid flow over thin moving needle subject to Arrhenius activation energy, viscous dissipation and binary chemical reaction. Case Stud. Therm Eng. 2021;25:100989.
[10] Choi SUS. Enhancing thermal conductivity of fluids with nanoparticles. Am Soc Mech Eng Fluids Eng Div FED. 1995;231:99–105.
[11] Varun Kumar RS, Gunderi Dhananjaya P, Naveen Kumar R, Punith Gowda RJ, Prasannakumara BC. Modeling and theoretical investigation on Casson nanofluid flow over a curved stretching surface with the influence of magnetic field and chemical reaction. Int J Comput Methods Eng Sci Mech. 2022;23:12–9.
[12] Acharya N, Mabood F, Shahzad SA, Badruddin IA. Hydrothermal variations of radiative nanofluid flow by the influence of nanoparticles diameter and nanolayer. Int Commun Heat Mass Transf. 2022;130:105781.
[13] Shahid A, Bhatti MM, Ellahi R, Mekheimer KS. Numerical experiment to examine activation energy and bi-convection Carreau nanofluid flow on an upper paraboloid porous surface: Application in solar energy. Sustain Energy Technol Assess. 2022;52:102029.
[14] Khan A, Alyami MA, Alghamdi W, Alqarni MM, Yassen MF, Tag Eldin E. Thermal examination for the micropolar gold–blood nanofluid flow through a permeable channel subject to gyrotactic microorganisms. Front Energy Res. 2022;10:993247.
[15] Bhatti MM, Arain MB, Zeeshan A, Ellahi R, Doranehgard MH. Swimming of Gyrotactic Microorganism in MHD Williamson nanofluid flow between rotating circular plates embedded in porous medium: Application of thermal energy storage. J Energy Storage. 2022;45:103511.
[16] Waqas H, Wakif A, Al-Mdallal Q, Zaydan M, Farooq U, Hussain M. Significance of magnetic field and activation energy on the features of stratified mixed radiative-convective couple-stress nanofluid flows with motile microorganisms. Alex Eng J. 2022;61:1425–36.
[17] Anjum N, Khan WA, Azam M, Ali M, Waqas M, Hussain I. Significance of bioconvection analysis for thermally stratified 3D Cross nanofluid flow with gyrotactic microorganisms and activation energy aspects. Therm Sci Eng Prog. 2023;38:101596.

[18] Upreti H, Pandey AK. MHD Tangent Hyperbolic Fluid Flow Over Stretching Sheet with Cattaneo–Christov Heat Flux Model and Quadratic Convection: A Statistical Analysis. Math Model Fluid Dyn Nanofluids. CRC Press; p. 84–100.
[19] Upreti H, Mishra SR, Kumar Pandey A, Joshi N, Joshi BP. Diversified role of fuzzified particle concentration on Casson gold-blood nanofluid flow through an elongating sheet for different shape nanoparticles. J Taibah Univ Sci. 2023;17:2254465.
[20] Upreti H, Mishra SR, Pandey AK, Bartwal P. Shape factor analysis in stagnation point flow of Casson nanofluid over a stretching/shrinking sheet using Cattaneo–Christov model. Numer Heat Transf Part B Fundam. 2023;1–17.
[21] Pandey AK, Upreti H. Heat and mass transfer in convective flow of nanofluid. Adv Math Comput Model Eng Syst. CRC Press; 2023. p. 295–313.
[22] Rasheed T, Hussain T, Anwar MT, Ali J, Rizwan K, Bilal M, Alshammari FH, Alwadai N, Almuslem AS. Hybrid nanofluids as renewable and sustainable colloidal suspensions for potential photovoltaic/thermal and solar energy applications. Front Chem. 2021;9:737033.
[23] Sundar LS, Shaik F. Heat transfer and exergy efficiency analysis of 60% water and 40% ethylene glycol mixture diamond nanofluids flow through a shell and helical coil heat exchanger. Int J Therm Sci. 2023;184:107901.
[24] Wang X, Wen Q, Yang J, Shittu S, Wang X, Zhao X, Wang Z. Heat transfer and flow characteristic of a flat confined loop thermosyphon with ternary hybrid nanofluids for electronic devices cooling. Appl Therm Eng. 2023;221:119758.
[25] Adun H, Kavaz D, Dagbasi M. Review of ternary hybrid nanofluid: Synthesis, stability, thermophysical properties, heat transfer applications, and environmental effects. J Clean Prod. 2021;328:129525.
[26] Mahmood Z, Khan U, Saleem S, Rafique K, Eldin SM. Numerical analysis of ternary hybrid nanofluid flow over a stagnation region of stretching/shrinking curved surface with suction and Lorentz force. J Magn Magn Mater. 2023;573:170654.
[27] Atashafrooz M, Sajjadi H, Delouei AA. Simulation of combined convective-radiative heat transfer of hybrid nanofluid flow inside an open trapezoidal enclosure considering the magnetic force impacts. J Magn Magn Mater. 2023;567:170354.
[28] Raizah Z, Khan A, Gul T, Saeed A, Bonyah E, Galal AM. Coupled Dufour and Soret Effects on Hybrid Nanofluid Flow through Gyrating Channel Subject to Chemically Reactive Arrhenius Activation Energy. J Nanomater. 2023;2023:2023–13.
[29] Latha KBS, Reddy MG, Tripathi D, Bég OA, Kuharat S, Ahmad H, et al. Computation of stagnation coating flow of electro-conductive ternary Williamson hybrid GO-AU-Co_3O_4/EO nanofluid with a Cattaneo–Christov heat flux model and magnetic induction. Sci Rep. 2023;13:10972.
[30] Prakash J, Tripathi D, Bég OA. Computation of EMHD ternary hybrid non-Newtonian nanofluid over a wedge embedded in a Darcy-Forchheimer porous medium with zeta potential and wall suction/injection effects. Int J Ambient Energy. 2023;44:1–15.
[31] Butt AW, Akbar NS, Tripathi D, Akram J. Analytical Investigation of Electroosmotically Regulated Peristaltic Propulsion of Cu-water Nanofluid Through a Microtube. Iraqi J Sci. 2023;2354–67.
[32] Munawar S, Saleem N, Tripathi D. Cilia and electroosmosis induced double diffusive transport of hybrid nanofluids through microchannel and entropy analysis. Nonlinear Eng. 2023;12:20220287.
[33] Bhandari DS, Tripathi D. Study of entropy generation and heat flow through a microtube induced by the membrane-based thermofluidics systems. Therm Sci. Eng Prog. 2022;34:101395.
[34] Akram J, Akbar NS, Alansari M, Tripathi D. Electroosmotically modulated peristaltic propulsion of TiO_2/10W40 nanofluid in curved microchannel. Int Commun Heat Mass Transf. 2022;136:106208.
[35] Akram J, Akbar NS, Tripathi D. A theoretical investigation on the heat transfer ability of water-based hybrid (Ag–Au) nanofluids and Ag nanofluids flow driven by electroosmotic pumping through a microchannel. Arab J Sci Eng. 2021;46:2911–27.
[36] Sridhar V, Ramesh K, Tripathi D, Vivekanand V. Analysis of thermal radiation, Joule heating, and viscous dissipation effects on blood-gold couple stress nanofluid flow driven by electroosmosis. Heat Transf. 2022;51:4080–101.
[37] Abdal S, Siddique I, Afzal S, Sharifi S, Salimi M, Ahmadian A. An analysis for variable physical properties involved in the nano-bio-film transportation of sutterby fluid across shrinking/stretching surface. Nanomaterials. 2022;12:599.
[38] Bilal S, Ali Shah I, Akgül A, Taştan Tekin M, Botmart T, Sayed Yousef E, et al. A comprehensive mathematical structuring of magnetically effected Sutterby fluid flow immersed in dually stratified medium under boundary layer approximations over a linearly stretched surface. Alex Eng J. 2022;61:11889–98.
[39] Bhatti MM, Shahid A, Sarris IE, Anwar Bég O. Spectral relaxation computation of Maxwell fluid flow from a stretching surface with quadratic convection and non-Fourier heat flux using Lie symmetry transformations. Int J Mod Phys B. 2023;37:2350082.
[40] Alqahtani AM, Bilal M, Usman M, Alsenani TR, Ali A, Mahmuod SR. Heat and mass transfer through MHD Darcy Forchheimer Casson hybrid nanofluid flow across an exponential stretching sheet. ZAMM-J Appl Math Mech für Angew Math und Mech. 2023;103:e202200213.
[41] Noor Amalina Nisa A, Iskandar W, Abdul Rahman Mohd K, Mohamad Hidayad Ahmad K, Mohd Rijal A, Seripah Awang K. Flow and heat transfer analysis on Reiner-Philippoff fluid flow over a stretching sheet in the presence of first and second order velocity slip and temperature jump effects. CFD Lett. 2023;15:88–102.
[42] Mahabaleshwar US, Maranna T, Pérez LM, Ravichandra Nayakar SN. An effect of magnetohydrodynamic and radiation on axisymmetric flow of non-Newtonian fluid past a porous shrinking/stretching surface. J Magn Magn Mater. 2023;571:170538.
[43] Sharma BK, Khanduri U, Mishra NK, Mekheimer KS. Combined effect of thermophoresis and Brownian motion on MHD mixed convective flow over an inclined stretching surface with radiation and chemical reaction. Int J Mod Phys B. 2022;2350095.
[44] Hussain M, Sheremet M. Convection analysis of the radiative nanofluid flow through porous media over a stretching surface with inclined magnetic field. Int Commun Heat Mass Transf. 2023;140:106559.
[45] Flaman GT, Boyle ND, Vermelle C, Morhart TA, Ramaswami B, Read S, et al. Chemical Imaging of Mass Transport Near the No-Slip Interface of a Microfluidic Device using Attenuated Total Reflection–Fourier Transform Infrared Spectroscopy. Anal Chem. 2023;95:4940–9.
[46] Asghar A, Chandio AF, Shah Z, Vrinceanu N, Deebani W, Shutaywi M, et al. Magnetized mixed convection hybrid nanofluid with effect of heat generation/absorption and velocity slip condition. Heliyon. 2023;9:9.

[47] Patel VK, Pandya JU, Patel MR. Testing the influence of TiO_2– Ag/ water on hybrid nanofluid MHD flow with effect of radiation and slip conditions over exponentially stretching & shrinking sheets. J Magn Magn Mater. 2023;572:170591.

[48] Zainodin S, Jamaludin A, Nazar R, Pop I. Effects of higher order chemical reaction and slip conditions on mixed convection hybrid ferrofluid flow in a Darcy porous medium. Alex Eng J. 2023;68:111–26.

[49] Mahmood Z, Eldin SM, Rafique K, Khan U. Numerical analysis of MHD tri-hybrid nanofluid over a nonlinear stretching/shrinking sheet with heat generation/absorption and slip conditions. Alex Eng J. 2023;76:799–819.

[50] Yasin M, Hina S, Naz R, Abdeljawad T, Sohail M. Numerical Examination on impact of hall current on peristaltic flow of eyring-powell fluid under ohmic-thermal effect with slip conditions. Curr Nanosci. 2023;19:49–62.

[51] Ramzan M, Shahmir N, Saleel CA, Kadry S, Eldin SM, Saeed AM. Model-based comparison of hybrid nanofluid Darcy-Forchheimer flow subject to quadratic convection and frictional heating with multiple slip conditions. Numer Heat Transf Part A Appl. 2023;1–21.

[52] Shahzadi I, Duraihem FZ, Ijaz S, Raju CSK, Saleem S. Blood stream alternations by mean of electroosmotic forces of fractional ternary nanofluid through the oblique stenosed aneurysmal artery with slip conditions. Int Commun Heat Mass Transf. 2023;143:106679.

[53] Ashraf M, Ashraf MM. MHD stagnation point flow of a micropolar fluid towards a heated surface. Appl Math Mech. 2011;32:45–54.

[54] Das K. Slip effects on MHD mixed convection stagnation point flow of a micropolar fluid towards a shrinking vertical sheet. Comput Math Appl. 2012;63:255–67.

[55] Venkateswarlu B, Satya Narayana PV. Cu-Al_2O_3/H_2O hybrid nanofluid flow past a porous stretching sheet due to temperature-dependent viscosity and viscous dissipation. Heat Transf. 2021;50:432–49.

[56] Wakif A, Chamkha A, Thumma T, Animasaun IL, Sehaqui R. Thermal radiation and surface roughness effects on the thermo-magneto-hydrodynamic stability of alumina–copper oxide hybrid nanofluids utilizing the generalized Buongiorno's nanofluid model. J Therm Anal Calorim. 2021;143:1201–20.

[57] Dawar A, Islam S, Shah Z, Mahmuod SR, Lone SA. Dynamics of inter-particle spacing, nanoparticle radius, inclined magnetic field and nonlinear thermal radiation on the water-based copper nanofluid flow past a convectively heated stretching surface with mass flux condition: A strong suction case. Int Commun Heat Mass Transf. 2022;137:106286.

[58] Dawar A, Thumma T, Islam S, Shah Z. Optimization of response function on hydromagnetic buoyancy-driven rotating flow considering particle diameter and interfacial layer effects: Homotopy and sensitivity analysis. Int Commun Heat Mass Transf. 2023 [cited 2023 Apr 9];144:106770. https://linkinghub.elsevier.com/retrieve/pii/S0735193323001598.

[59] Dawar A, Islam S, Shah Z, Mahmuod SR. A passive control of Casson hybrid nanofluid flow over a curved surface with alumina and copper nanomaterials: A study on sodium alginate-based fluid. J Mol Liq. 2023;382:122018.